Performance and application of a superlattice infrared photodetector with a blocking barrier

C. C. Chen, H. C. Chen, M. C. Hsu, W. H. Hsieh, C. H. Kuan, S. Y. Wang, and C. P. Lee

Citation: Journal of Applied Physics **91**, 943 (2002); doi: 10.1063/1.1430887
View online: http://dx.doi.org/10.1063/1.1430887
View Table of Contents: http://scitation.aip.org/content/aip/journal/jap/91/3?ver=pdfcov
Published by the AIP Publishing

Performance and application of a superlattice infrared photodetector with a blocking barrier

C. C. Chen, H. C. Chen, M. C. Hsu, W. H. Hsieh, and C. H. Kuan[a)]
Department of Electrical Engineering and Graduate Institute of Electronics Engineering, National Taiwan University, Taipei, Taiwan, Republic of China 10617

S. Y. Wang
Institute of Astronomy and Astrophysics Academia Sinica, Taipei, Taiwan, Republic of China 10617

C. P. Lee
Department of Electronic Engineering, National Chiao Tung University, Hsinchu, Taiwan, Republic of China 30050

(Received 7 June 2001; accepted for publication 3 November 2001)

An infrared photodetector that contains a superlattice structure and a blocking barrier was investigated. The photodetector shows advantages including a low operating voltage (<0.7 V), wide detection bandwidth, flexible miniband engineering, and in particular, voltage-tunable spectral responsivity. The blocking barrier not only prohibits the dark current but also acts as a high-pass energy filter to tune the spectral responsivity. The zero background peak detectivity of our detector is 3.7×10^{9} cm $\mathrm{Hz}^{0.5}$/W (9.7 μm) at -0.5 V and 2.2×10^{10} cm $\mathrm{Hz}^{0.5}$/W (6.7 μm) at -0.1 V. Since the spectral responsivity at different biases is independent, temperature sensing is feasible by taking the ratio of the measured photocurrent at different biases. A demonstration of temperature sensing by using our superlattice infrared photodetector with a blocking barrier is also shown in this article. Those results show the superlattice is a simple and efficient structure for the design of a multicolor infrared photodetector. © *2002 American Institute of Physics.* [DOI: 10.1063/1.1430887]

I. INTRODUCTION

The exploitation of a superlattice-based structure for infrared detection has drawn much attention since the first clear demonstration of quantum well infrared photodetectors (QWIPs).[1] For photovoltaic operation, the superlattice with a graded barrier, which was also called the Kastalsky-type photodetector, was fabricated to detect infrared radiation in the short wavelength region[2] (3.6–6.3 μm) and long wavelength region[3] (8–10.5 μm). Utilizing a flat blocking barrier to reduce the dark current, the superlattice detector operated at low bias region with spectral responsivity peak at 14.5 μm was demonstrated.[4] Besides, the superlattice alone was also shown to be applicable for the detection of infrared radiation in a broad wavelength region (5–10 μm).[5] Those earlier works on the superlattice infrared photodetectors indicate that the advantages of the superlattice-based infrared photodetector include a broader absorption spectrum, lower operating voltage, and more flexible miniband engineering than the conventional QWIP. However, no voltage-tunable spectral responsivity was reported in the previous works.

In this article, we design and survey a detector composed of a 14-period GaAs/$Al_{0.27}Ga_{0.73}As$ superlattice and a current blocking barrier for the detection of the ~10 μm wavelength light. The current blocking barrier not only reduces the dark current but also acts as a voltage-tuned high-pass energy filter for the photoexcited carriers. Therefore, the spectral responsivity is tunable by external bias and the multiwavelength operation is enabled for temperature sensing.

This article is organized as follows. Section I is a brief introduction. Then the structure and performances, which include the absorption spectrum, current–voltage relation, noise performance, responsivity, and detectivity of the superlattice detector, are presented in Sec. II. Section III is a detailed discussion underneath the observed voltage-dependent spectral responsivity. In Sec. IV, temperature sensing by using our superlattice infrared photodetector is demonstrated. The last section is the summary of this article.

II. STRUCTURE AND CHARACTERISTICS OF THE DETECTOR

A. Detector structure

The schematic band diagram of the superlattice infrared photodetector is shown in Fig. 1. The structure, grown by molecular beam epitaxy on a semi-insulating GaAs substrate, contains a 500 nm heavily doped GaAs bottom contact layer, a 150 nm $Al_{0.23}Ga_{0.77}As$ current blocking barrier, a 14-period GaAs/$Al_{0.27}Ga_{0.73}As$ superlattice, and a 400 nm heavily doped top contact layer. The contact layers are both doped with 1×10^{18} cm^{-3} of Si. Each period of the superlattice consists of 6.5 nm GaAs well doped with 5×10^{17} cm^{-3} of Si and 3.5 nm undoped $Al_{0.27}Ga_{0.73}As$ barrier. The shadowed region in Fig. 1 shows the two minibands formed in the superlattice structure. Each miniband contains 14 resonant-tunneling states. The conduction band offset of $Al_xGa_{1-x}As$ relative to GaAs is taken as $810x$ meV. Relative to the conduction band edge of GaAs, the first miniband ranges from 47 to 60 meV and the second miniband ranges from 174 to 242 meV.

a)Electronic mail: kuan@cc.ee.ntu.edu.tw

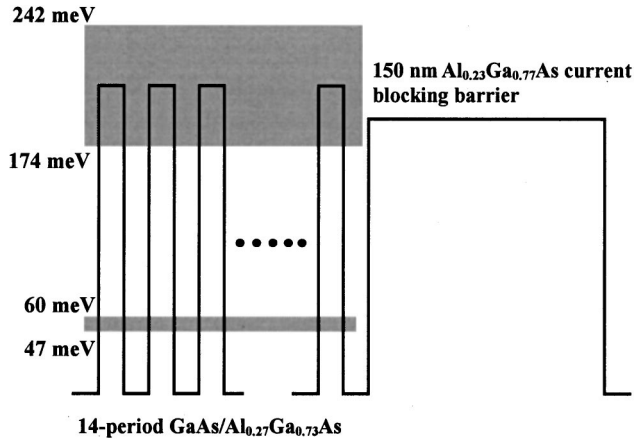

FIG. 1. Schematic band diagram of the superlattice infrared photodetector. The superlattice is composed of 6.5 nm GaAs well and 3.5 nm $Al_{0.27}Ga_{0.73}As$ barrier. The 150 nm $Al_{0.23}Ga_{0.77}As$ current blocking barrier and the superlattice barriers are both undoped and the GaAs well region of the superlattice is doped with 5×10^{17} cm^{-3} of Si. From the conduction band edge of the GaAs, two minibands are formed that range from 47 to 60 and 174 to 242 meV, respectively.

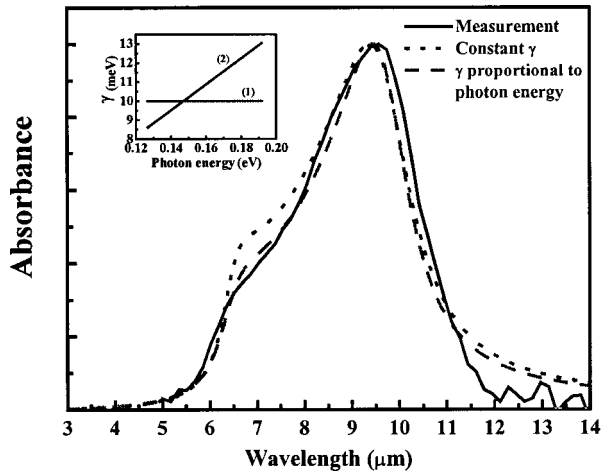

FIG. 2. Measured and calculated absorption spectrum for the TM-polarized light incident upon the superlattice structure. The measured data is represented by the solid curve. The dotted curve is calculated with γ equal to 10 meV as indicated by (1) in the inset, and the dashed curve is calculated with γ (8.6–13 meV) proportional to the photon energy as indicated by (2) in the inset.

In order to make the spectral responsivity tunable by external bias and block the dark current, a current blocking barrier that serves as a voltage-tuned high-pass energy filter for the photoelectrons is introduced. The barrier height (186 meV) is designed to be higher than the bottom state of the second miniband in the superlattice. At around zero bias, photoelectrons with energy higher than the blocking barrier can pass through it, while photoelectrons with energy lower are blocked. At high biases, due to the assistance of the strong electric field on the blocking barrier, part of the blocked photoelectrons can tunnel through the current blocking barrier and contribute to the photocurrent. As a result, the long-wavelength responsivity, corresponding to the excitation of the carriers to the bottom state of the second miniband, indeed appears at high bias region along with the short-wavelength one. On the other hand, only the short-wavelength peak is observed at low bias region.

The device was fabricated into a 200×400 μm^2 mesa by standard photolithography, chemical wet etching, evaporation, and lift-off processes. The top and bottom contacts were made by evaporating 100 nm Ni/Ge/Au and 200 nm Au. After evaporation and lift-off, thermal annealing at 390 °C was performed to make ohmic contact with the n^+ contact layer in the semiconductor. Finally, a 45° facet on the substrate was polished to allow the detector to probe the TM polarized infrared radiation.

B. Detector performance

1. Absorption

The energy position of the superlattice miniband relative to the barrier height affects the tunneling probability of the photoelectrons and is important to the voltage-tunable spectral responsivity. Therefore, the absorption spectrum of the sample was performed in order to confirm the formation and position of the miniband structure. Since only the TM-polarized light can be absorbed in the superlattice structure, the sample was prepared as a waveguide geometry with parallel 45° facets at both ends. Both sides of the waveguide were polished to confine light in the waveguide region by total reflection. The absorption spectrum was measured by Fourier-transform infrared spectrometer and the resulting absorbance for the TM-polarized light is shown as the solid curve in Fig. 2. In the absorption spectrum, there is a peak at 9.7 μm and a shoulder at around 6.7 μm which correspond to the transitions near zone edge and zone center of the superlattice structure.[6] A theoretical calculation of the absorption spectrum to fit the measurement data is also shown in Fig. 2. The details of calculating the absorption spectrum will be presented later in Sec. III A.

2. Dark current and photocurrent

Shown in Fig. 3 are dark currents at various temperatures as represented by the solid curves and 300 K background photocurrent of the detector at 20 K as represented

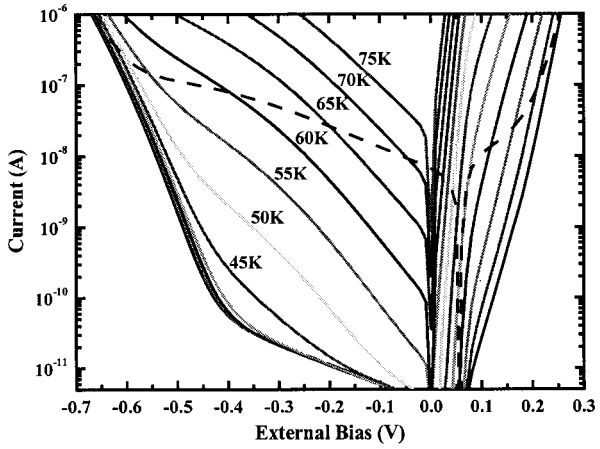

FIG. 3. The $I-V$ characteristics of our detector. The solid curves represent the dark current at various temperatures ranging from 20 to 75 K and the dashed curve represents the 300 K background photocurrent for the detector at 20 K.

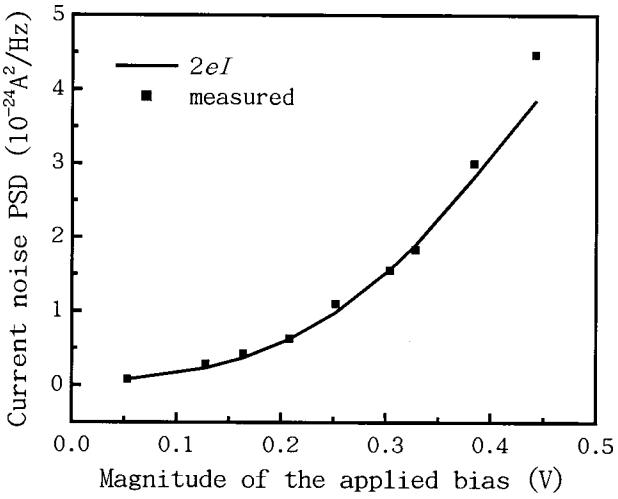

FIG. 4. The power spectral density of the current noise vs the external bias for our detector at 77 K. The solid curve is the calculated shot noise $2eI$ from the dark current at 77 K, and the solid squares are the measured data with sample immersed in 77 K liquid nitrogen.

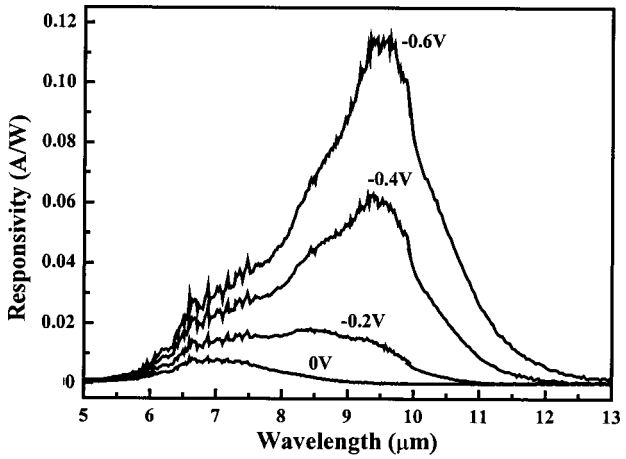

FIG. 5. Spectral responsivity from 0 to -0.6 V at various biases at 25 K. The responsivity at 9.7 μm is suppressed at zero bias, while it increases with applied bias and dominates the spectral responsivity at -0.6 V.

by the dashed curve. The voltage polarity is defined as positive if a high potential is applied on the top contact. The dark current of the detector is asymmetric with the voltage polarity and the large dark current at the positive bias is attributed to the dopant migration from the bottom contact to the current blocking barrier.[7,8] Then, in the rest of this article, only a negative bias region is considered. It is observed from the comparison between the dashed and solid curve that the temperature range with background limited operation of the detector is below 55 K when the detector is biased at -0.5 V, and 65 K at -0.2 V. For the operation with background limited performance in the bias range between 0 and -0.5 V, the detector should be cooled below 55 K.

3. Noise

The noise measurement was proceeded with the sample immersed in 77 K liquid nitrogen and is shielded to prevent illumination of the room-temperature infrared radiation. The current noise of the detector was amplified by a low noise current amplifier and was extracted carefully from the inevitable noise sources of the amplifier. The detailed setup for noise measurement can be found in our previous article.[9] The frequency range of the noise measurement is from dc to 10 kHz and limited by the amplifier bandwidth. It is observed that the measured current noise is white noise in the frequency range, and the current noise power spectral density matches well with the shot noise $2eI$ of the dark current at 77 K as shown in Fig. 4. Thus, the noise performance of the detector is attributed to the thermally assisted tunneling of the electrons through the edge tip of the blocking barrier, and is consistent with the dominant mechanism of the dark current.

4. Responsivity and detectivity

The spectral responsivity at various temperatures and biases was measured with a monochromator and a lock-in amplifier. A glowbar radiator was used as the light source and the wavelength was selected with the monochromator. The peak responsivity was calibrated with a blackbody radiation source heated to 500 °C.[10,11] The observed spectral responsivity shows little temperature dependence, and the representative one at 25 K is shown in Fig. 5. It is clear that at zero bias, the detected wavelength is primarily at 6.7 μm. While the negative bias increases in magnitude, another peak at 9.7 μm rises and dominates the spectral responsivity at a high bias region. Therefore, the spectral responsivity is tunable by an external bias between 6.7 and 9.7 μm, which allows the detector to be applicable in versatile applications including temperature sensing and target recognition. This experimental result agrees with the design principle mentioned at Sec. II A.

The detectivity, which is a figure of merit to evaluate the detector, is given by

$$D^*(\lambda,f)=\frac{\sqrt{A_d\Delta f}}{i_{\mathrm{rms}}}R(\lambda), \tag{1}$$

where A_d is the area of the detector, f is the chopper frequency, Δf is the bandwidth of measurement, $R(\lambda)$ is the spectral responsivity, and i_{rms} is the current noise of the detector. As mentioned earlier, the current noise matches well with the shot noise of dark current at 77 K. Thus, the current noise in Eq. (1) is estimated with the assumption that the current noise is also the shot noise at other temperatures because the dark current is primarily dominated by the thermally assisted tunneling. Therefore, the dark current limited zero background peak detectivity,[12] D^* (9.7 μm, 100 Hz) is 3.7×10^9 cm Hz$^{0.5}$/W at -0.5 V and D^* (6.7 μm, 100 Hz) is 2.2×10^{10} cm Hz$^{0.5}$/W at -0.1 V at 45 K. Based on the detectivity, the superlattice infrared photodetector has compatible performance with the QWIP.

In brief, compared with the QWIP, the detector shows a lower operating voltage, and broader and tunable spectral responsivity, which makes our detector an attractive two-color photodetector with peaks at 6.7 and 9.7 μm. In the next section, the calculation of the absorption spectrum will be presented and the voltage-dependent spectral responsivity

will be discussed. In Sec. IV, we will show the feasibility of the detector as a temperature sensor by making use of the voltage-tuned spectral responsivity.

III. DISCUSSION

Our photodetector relies primarily on the miniband transition in the superlattice structure to transform infrared radiation into photoelectrons that can conduct electrical current. It is essential to discuss both the miniband transition and transport of the photoelectrons in detail. In the following, the calculation of the superlattice absorption spectrum will be presented in Sec. III A. The miniband structure was extracted from the fitting of the absorption spectrum. The transport of the photoelectrons through the superlattice and the blocking barrier will be taken into account to explain the voltage-dependent spectral responsivity in Sec. III B.

A. Absorption coefficient

In the following calculation, we adopt a periodical boundary condition and calculate the absorption spectrum by counting the contributions from the 14 resonant-tunneling states in the miniband. However, it is observed from Figs. 2 and 5 that neither the measured absorption spectrum nor the spectral responsivity show the fine structure originated from the 14 discrete transitions. It is attributed to the fact that each discrete transition is broadened with a bandwidth comparable to the energy separation between the neighboring states. In the following analysis, the Lorentzian broadening line shape is assumed.

The selection rule for the superlattice miniband transition allows the electrons in the resonant-tunneling state $\Psi_{N+1-p}^{1\mathrm{st}}$ in the first miniband to be excited to the corresponding resonant-tunneling state $\Psi_p^{2\mathrm{nd}}$ in the second miniband by absorbing infrared light.[6] The energies and the corresponding wave functions of the resonant-tunneling states were calculated by using the transfer matrix method. The overall absorption coefficient resulting from each individual transition from the first to the second miniband is given by[13,14]

$$\alpha(\lambda)=\sum_p \frac{e^2kT}{\epsilon_0 cn\hbar^2\pi m^*\omega_p}\left|\langle\Psi_p^{2\mathrm{nd}}|p_z|\Psi_{N+1-p}^{1\mathrm{st}}\rangle\right|^2 \times\ln\left\{\frac{1+\exp[(E_f-E_{N+1-p}^{1\mathrm{st}})/kT]}{1+\exp[(E_f-E_p^{2\mathrm{nd}})/kT]}\right\} \cdot\frac{\gamma/\pi}{(E_p^{2\mathrm{nd}}-E_{N+1-p}^{1\mathrm{st}}-hc/\lambda)^2+\gamma^2}, \quad (2)$$

where n is the refractive index, m^* is the effective mass, ω_p is the angular frequency of photon with energy $E_p^{2\mathrm{nd}}-E_{N+1-p}^{1\mathrm{st}}$, and γ is the Lorentzian broadening factor. Figure 2 shows the measured absorption spectrum along with two curves calculated with the γ values shown in the inset. The dotted curve is calculated with γ value equal to 10 meV,[15] and the dashed curve is with γ (8.6–13 meV) proportional to the photon energy. Comparing the dotted and dashed curves, the shoulder and peak positions are consistent with the experiment in both cases, but the relative magnitude to the experiment at the shoulder is larger for the dotted curve. This reflects the tendency that the broadening of the higher-energy transition is larger than the lower-energy one. Since the peak and shoulder positions are not affected by the γ value, the miniband structure established by fitting the peak and shoulder positions is the same in both cases. As a result, the first miniband ranges from 53 to 62 meV and the second one from 188 to 245 meV. Compared with those shown in Fig. 1, the well and barrier widths extracted from the fitting are 6.1 and 4.4 nm, respectively. Their difference between the nominal and extracted values is caused by the deviations of the actual growth rates. In addition, the nominal barrier height of the blocking barrier is a little bit lower than the actual bottom state of the second miniband in the superlattice. Although this result contradicts our design, yet the actual barrier height is higher than the bottom state and the associated evidence will be shown and discussed in the following subsection.

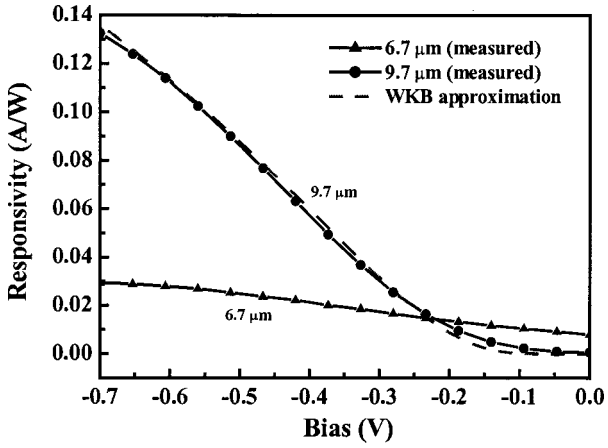

FIG. 6. Responsivity vs bias. The solid circles and triangles are the measured voltage dependences of responsivity at 6.7 and 9.7 μm. The dashed curve is the tunneling probability calculated by the WKB method with photoelectron energy 18.7 meV lower than the blocking barrier.

B. Voltage-dependent spectral responsivity

In order to investigate the actual barrier height and the transport mechanism of the photoelectrons, the spectral responsivity versus applied bias for the monochromatic wavelengths, 6.7 and 9.7 μm, is measured and shown in Fig. 6. The former (latter) wavelength is associated with the shoulder (peak) and corresponds to the transition from the first miniband to the top (bottom) state of the second miniband. The responsivity for 6.7 μm increases slowly with the bias while that for 9.7 μm is almost zero for the bias magnitude less than 0.1 V and increases dramatically beyond 0.2 V.

Under the assumption that the actual barrier height of the blocking barrier is higher than the bottom state of the second miniband in the superlattice, the experimental results can be understood with the schematic drawings of the band diagrams and photoelectron distributions shown in Fig. 7. For the 9.7 μm wavelength detection, the photoelectrons are accumulated in the bottom state of the second miniband and cannot tunnel through the blocking barrier under low biases as shown in Fig. 7(a). When the bias increases, the tunneling path decreases as shown in Fig. 7(b) and the associated prob-

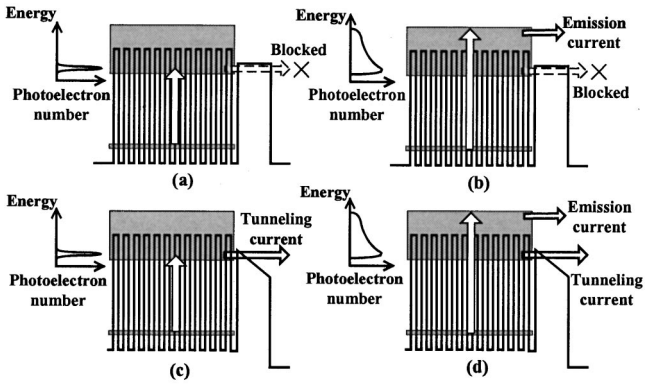

FIG. 7. Schematic illustrations of photoelectron transport in our detector (a) under zero bias and illuminated by 9.7 μm light; (b) under high bias and illuminated by 9.7 μm light; (c) under zero bias and illuminated by 6.7 μm light; (d) under high bias and illuminated by 6.7 μm light.

ability increases dramatically as implied in the spectral responsivity for the 9.7 μm in Fig. 6. In order to verify the tunneling behavior, the tunneling probability calculated with the Wentzel–Kramers–Brillouin (WKB) method is shown as the dashed curve in Fig. 6. In the calculation, the blocking barrier is 18.7 meV higher than the photoelectron energy. The agreement of the dashed curve and the solid circles confirms the model shown in Figs. 7(a) and 7(b). It is therefore concluded that the actual barrier height is 206 meV instead of 186 meV, and the associated aluminum fraction of the blocking barrier is $x=0.258$. This value is 12% higher than the nominal value and is within the accuracy of the epilayer growth in our molecular beam epitaxy system.

On the other hand, for the 6.7 μm wavelength detection, the photoelectrons are not accumulated in the top state of the second miniband but distributed incrementally as their energy decreases because of the intraminiband relaxation as shown in Figs. 7(c) and 7(d). Even at zero bias, the photoelectrons with energy higher than the barrier height can pass through the blocking barrier as shown in Fig. 7(c). The dominant photocurrent is so called the emission current. As the applied bias increases, the number of the photoelectrons, which can pass through the blocking barrier, increases due to the increasing tunneling current as shown in Fig. 7(d). Because of the broad unknown photoelectron distribution, it is difficult to calculate the corresponding bias dependence of the responsivity. However, the picture of the emission and tunneling currents in Fig. 7 can explain the responsivity versus bias for the 6.7 μm. In addition, since the energy of the photoelectrons for the 6.7 μm is higher than that for the 9.7 μm, the relaxation rate of the former photoelectrons is in general expected to be higher than that of the latter. This is consistent with the tendency of the broadening factor γ of the absorption spectrum as discussed in Sec. III A.

For the detection of the wavelength between 6.7 and 9.7 μm, the resulted photoelectron distribution is between those two shown in Fig. 7. As the detected wavelength increases from 6.7 μm, the highest energy of the photoelectron distribution decreases. The ultimate distribution is the one for the 9.7 μm. For the illumination of a specific wavelength, the emission current is determined by those photoelectrons in the associated distribution whose energy is higher than the barrier height of the blocking barrier. As the bias increases, the additional tunneling current increases and may surpass the emission current as the example of the 9.7 μm case. Therefore, the blocking barrier acts as a high-pass energy filter and causes the tunability of the spectral responsivity. In the following, we will take advantage of that characteristic and demonstrate the feasibility of temperature sensing with our detector.

IV. TEMPERATURE SENSING

The photocurrent measured by a detector with the spectral responsivity $R(\lambda)$ of a gray body at temperature T can be expressed as the integral of the thermal radiation falling on a detector multiplying the spectral responsivity of the detector

$$I_p=\int \epsilon \frac{L_{\mathrm{BB}}(\lambda,T)A_sA_d}{r^2}R(\lambda)d\lambda, \tag{3}$$

where ϵ is the emissivity of the gray body, $L_{\mathrm{BB}}(\lambda,T)$ is the standard blackbody spectral radiance at temperature T, r is the distance between the source and the detector, and $A_{s(d)}$ is the area of the source (detector). Here we assume that no absorption occurs at the radiation path. The standard blackbody spectral radiance is described by the Planck's law

$$L_{\mathrm{BB}}(\lambda,T)=\frac{2\pi hc^2}{\pi\lambda^5[\exp(hc/\lambda kt)-1]}=\frac{1.19\times10^4}{\lambda^5\left[\exp\left(\frac{14\,404}{\lambda T}\right)-1\right]}, \tag{4}$$

where the unit of $L_{\mathrm{BB}}(\lambda,T)$ is watt per steradiance per square centimeter of area and per micrometer of radiation wavelength ($\mathrm{W\,sr^{-1}\,cm^{-2}\,\mu m^{-1}}$), λ is wavelength in micrometers, and T is temperature in kelvin. The target temperature cannot be extracted from the magnitude of measured photocurrent by a detector with only one spectral responsivity because the unknown parameters ϵ, r, and $A_{s(d)}$, which are related with the material property and the measurement configuration, are difficult to measure or control. By the use of two linearly independent spectral responsivities $R_1(\lambda)$ and $R_2(\lambda)$, the photocurrent ratio[16] (P_r) is defined as the ratio of the measured photocurrents I_{p1} and I_{p2}:

$$P_r(T)=\frac{I_{p1}}{I_{p2}}=\frac{\int L_{\mathrm{BB}}(\lambda,T)R_1(\lambda)d\lambda}{\int L_{\mathrm{BB}}(\lambda,T)R_2(\lambda)d\lambda}. \tag{5}$$

Since the unknowns ϵ, r, and $A_{s(d)}$ are eliminated, the resulting photocurrent ratio is a function of the target temperature only. Thus, the target temperature can be determined without preknowing ϵ, r, and $A_{s(d)}$, if ϵ is assumed to be independent of λ. The measuremed photocurrent ratio by using spectral responsivity at 0 and -0.5 V with a blackbody radiation source heated from 50 to 800 °C is shown as the solid dots in Fig. 8, and the solid curve is the predicted one. The difference between the experiment and prediction of the photocurrent ratio is due to the temperature fluctuation of the blackbody radiation source. However, from the agreement of the prediction and measurement, it is concluded that the detector

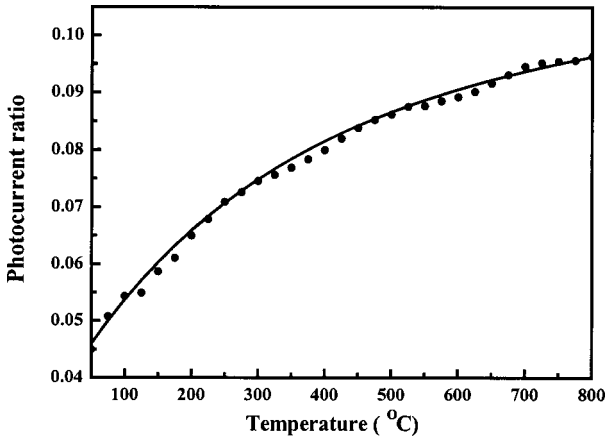

FIG. 8. Measured and estimated photocurrent ratio of spectral responsivities at 0 and −0.5 V. The solid dots are measured by using a blackbody radiation source from 100 to 800 °C and the solid curve is the calculated data.

is applicable in temperature sensing, especially in the vacuum chamber where there is no absorption during the radiation path.

V. SUMMARY

We have investigated and discussed the performance of the superlattice infrared photodetector with a blocking barrier. In addition to the advantages of low operating voltage (0 to 0.7 V), wide responsivity, and flexible miniband engineering, the detector also shows the tunability of the spectral responsivity with applied bias. The zero background peak detectivity of our detector is 3.7×10^{9} cm $Hz^{0.5}$/W (9.7 μm) at −0.5 V and 2.2×10^{10} cm $Hz^{0.5}$/W (6.7 μm) at −0.1 V at 45 K. Because of the voltage-tunable responsivity, the detector is applicable in various applications. In this article, temperature sensing by using the photocurrent ratio is demonstrated. All of the results show that the superlattice structure is an efficient and flexible structure in the design of infrared photodetectors.

ACKNOWLEDGMENT

This project is supported by the National Science Council in Taiwan under Contract No. of NSC 89-2215-E-002-058.

[1] B. F. Levine, K. K. Choi, C. G. Bethea, J. Walker, and R. J. Malik, Appl. Phys. Lett. **50**, 1092 (1987).
[2] A. Kastalsky, T. Duffield, S. J. Allen, and J. Harbison, Appl. Phys. Lett. **52**, 1320 (1988).
[3] O. Byungsung, J.-W. Choe, M. H. Francombe, K. M. S. V. Bandara, and D. D. Coon, Appl. Phys. Lett. **57**, 503 (1990).
[4] K. M. S. V. Bandara, J.-W. Choe, and M. H. Francombe, Appl. Phys. Lett. **60**, 3022 (1992).
[5] S. D. Gunapala, B. F. Levine, and N. Chand, J. Appl. Phys. **70**, 305 (1991).
[6] M. Helm, Semicond. Sci. Technol. **10**, 557 (1995).
[7] Y. H. Wang and S. S. Li, Appl. Phys. Lett. **62**, 93 (1993).
[8] *Quantum Well Intersubband Transition Physics and Devices*, edited by H. C. Liu, B. F. Levine, and J. Y. Anderson (Kluwer, Dordrecht, 1994), p. 29.
[9] C.-Y. Chen and C.-H. Kuan, IEEE Trans. Instrum. Meas. **49**, 77 (2000).
[10] E. L. Dereniak and D. G. Crowe, *Optical Radiation Detectors* (Wiley & Sons, New York, 1984), Chapts. 2–5.
[11] Richard D. Hudson, Jr., *Infrared System* (Wiley & Sons, New York, 1969), Chap. 9.
[12] S. D. Gunapala *et al.*, IEEE Trans. Electron Devices **47**, 963 (2000).
[13] M. Helm, W. Hilber, and T. Fromherz, Phys. Rev. B **48**, 1601 (1993).
[14] S. Nojima, Phys. Rev. B **41**, 10214 (1990).
[15] *Quantum Well Intersubband Transition Physics and Devices*, edited by H. C. Liu, B. F. Levine, and J. Y. Anderson (Kluwer, Dordrecht, 1994), p. 291.
[16] C. J. Chen, K. K. Choi, M. Z. Tidrow, and D. C. Tsui, Appl. Phys. Lett. **68**, 1446 (1996).